Propeller Blade Design Thickness and Blockage Issues Due to Source-Induced Factors

by

David S. Hunt

Submitted to the Departments of Ocean Engineering and Mechanical Engineering
in partial fulfillment of the requirements for the degrees of

Naval Engineer

and

Master of Science in Mechanical Engineering

at the

MASSACHUSETTS INSTITUTE OF TECHNOLOGY

February 2001

© David S. Hunt, 2001. All rights reserved.

The author hereby grants to MASSACHUSETTS INSTITUTE OF TECHNOLOGY permission to reproduce and to distribute copies of this thesis document in whole or in part.

Signature of Author .....
Departments of Ocean Engineering and Mechanical Engineering
11 January 2001

Certified by .....
Justin E. Kerwin
Professor of Naval Architecture
Thesis Supervisor

Read by .....
Douglas P. Hart
Associate Professor of Mechanical Engineering
Thesis Reader

Accepted by .....
Nicholas M. Patrikalakis
Kawasaki Professor of Engineering
Chairman, Committee on Graduate Students
Department of Ocean Engineering

Accepted by .....
Ain A. Sonin
Chairman, Committee on Graduate Students
Department of Mechanical Engineering

20010323 068

DISTRIBUTION STATEMENT A
Approved for Public Release
Distribution Unlimited

Propeller Blade Design Thickness and Blockage Issues Due to Source-Induced Factors

by

David S. Hunt

Submitted to the Departments of Ocean Engineering and Mechanical Engineering
on 11 January 2001, in partial fulfillment of the
requirements for the degrees of
Naval Engineer
and
Master of Science in Mechanical Engineering

Abstract

A propeller lifting-surface design and analysis program is improved upon by implementing enhancements in the source distribution calculation to represent the blade thickness. It is recognized that the present method of setting the source line distribution representing blade thickness (currently based on linearized slender-body theory for an isolated foil section) may introduce significant errors. This is the case for propulsors with a combination of a large thickness/chord ratio (blockage effect) and numerous blades (cascade effect).

A source panel (area) method was developed to more accurately model these effects. This method uses the lattice structure of the current PBD-14 code from which to compute the source-induced velocity factors between the blades, hub, and duct, if present. Using the method of images allows the hub and duct to be modeled as panel images from the blade panels. The source-induced effects of the whole propulsor are accounted for by using a panel method to obtain a source distribution along the mean camber surface of the blade. Invoking the kinematic boundary condition on the true blade suction and pressure surfaces solves this system of linear equations, which represent the blade thickness distribution. This robust formulation assigns source strengths more accurately over a much larger range of thickness/chord ratios and increasing numbers of blades, as evidenced by a more accurate velocity streamline trace representation of the actual pressure and suction side surfaces of the blade. Experimental validation is demonstrated for open and ducted flow stators.

Thesis Supervisor: Justin E. Kerwin
Title: Professor of Naval Architecture

Contents

List of Figures

List of Tables

Acknowledgments

"We were born before the wind

Also younger than the sun

Ere the bonnie boat was won as we sailed into the mystic

Hark, now hear the sailors cry

Smell the sea and feel the sky

Let your soul and spirit fly into the mystic."

Van Morrison (1970)

For Cheryl, a supportive wife, Caitlin, an exceptional daughter who manages to show me how truly special each day is, and Andrew, a wonderful son.

Thanks to Professor Justin Kerwin and Dr. Todd Taylor for the supportive guidance and ideas that enabled me to complete this work. Also, thanks to the "propnuts" crew for their creative ideas and support during my time at MIT.

Support for this research was provided by the Office of Naval Research under contract N00014-95-1-0389.

Nomenclature

Mathematical Notation

A		area of quadrilateral panel (flat $z-plane$)
BB		blade-to-blade influence functions
DB		duct-to-blade influence functions
dR		radial difference between source element endpoints
ds		differential component of local coordinate position
dS		differential component on the blade surface
dx		axial distance between control points in a chordwise strip
dt	δt	differential thickness between control points in a chordwise strip
$ductrat$	$\frac{L_{bldelem}}{L_{ductelem}}$	duct element imaged source strength adjustment factor
D		propeller diameter
h_1, h_2	$\frac{\partial \mathbf{x}}{\partial s}$	metric coefficient
HB		hub-to-blade influence functions
HIF		horseshoe influence function matrix
$hubrat$	$\frac{L_{bldelem}}{L_{hubelem}}$	hub element imaged source strength adjustment factor
ℓ		pressure side of the blade (lower surface)
$L_{bldelem}$		length of blade source element
$L_{ductelem}$		length of blade duct element
$L_{hubelem}$		length of blade hub element
L_{total}		total length of a source element
m		mean camber surface of the blade
$\hat{\mathbf{n}}$		normal vector on a surface
$\mathbf{p}$		surface coordinate
P		arbitrary point in space
R		radial coordinate
$\mathbf{R}$	$\mathbf{x}(s_1, s_2) - \mathbf{x}(s_1', s_2')$	differential position vector
s_1, s_2		local coordinates
S		blades surface
SIF		source influence function matrix

S_w		wake surface created by horseshoe
$\hat{\mathbf{t}}$		tangential vector on a surface
u	$\frac{\partial \Phi}{\partial x}$	velocity associated with the x-coordinate
U_{in}		inflow velocity to the propeller
U_s		component of inflow velocity
v	$\frac{\partial \Phi}{\partial y}$	velocity associated with the y-coordinate
$\mathbf{V}_{eff}$		effective velocity
$\mathbf{V}_{ind}$		total induced velocity
		induced circumferential mean velocity
$\widetilde{\mathbf{V}}_{ind_{fluc}}$		fluctuating component of induced velocity
$\mathbf{V}_{total}$		total velocity
$V\gamma_s$		component of velocity due to vortices
$V\sigma_s$		component of velocity due to sources
w	$\frac{\partial \Phi}{\partial z}$	velocity associated with the z-coordinate
$\mathbf{x}$		surface coordinate vector for x, y, z
x		axial coordinate
y		vertical coordinate
z		z-coordinate
$+/-$		upper/lower blade surface (suction/pressure side)
α		angle of attack of propeller blade
Φ		potential
γ		vortex element strength (per unit length)
Γ		blade circulation
Ω		blade rotation rate ($\frac{rad}{\text{sec}}$)
σ_A		source panel distribution (per unit area)
σ		source strength distribution (2D sense)
σ_L		source line distribution (per unit length)
$\Sigma\sigma_{src}$		sum of positive source strengths
$\Sigma\sigma_{snk}$		sum of negative source strengths (sinks)
ΣA_{src}		sum of panel areas due to source strengths
ΣA_{snk}		sum of panel areas due to sink strengths

Abbreviations

CMV	circumferential mean velocity
horseshoe	a vortex structure composed of: a spanwise vortex, its shed chordwise vortices on the blade and in the transition wake, and the ultimate wake helices.
RANS	Reynolds-Averaged Navier Stokes

Chapter 1

Introduction

1.1 Overview

The goal of this research was to create a more accurate model which describes the true lifting surface of a propeller blade system. This system includes the interactions between the propeller blades and the hub, as well as the duct, if present. Since many current propeller system design trends include the use of a multiple-staged ducted propulsors, accurately modelling the effects of induced velocities between the different components of the propulsor are paramount to perform a good analysis. There are several numerical tools and techniques which accomplish this task sufficiently [1]:

1. Lifting-Line Methods
2. Vortex-Lattice Lifting-Surface Methods
3. Boundary Integral Equation Methods
4. Axisymmetric and Three Dimensional Reynolds Averaged Navier Stokes (RANS) Flow Solvers.

The vortex-lattice lifting-surface technique provides an accurate and robust method to examine the design [2] and analysis [3] of complex marine propulsors efficiently. Kerwin et al. [2] [3] developed such a lifting-surface technique which has been improved upon [4] [5] since its introduction.

The vortex-lattice lifting-surface technique is a potential flow method which does not fully describe what occurs within the propulsor system, like full viscous flow models. However, Kerwin et al. [4] developed a coupling procedure which uses the potential flow lifting-surface technique in conjunction with a RANS viscous flow solver. This coupled technique allows for multiple blade row analysis while providing an accurate model of the physical behavior of the system.

The linearized slender-body theory representation does not accurately model the flow over the propeller blades because it under predicts the effects of the thickness distribution of the propeller blades. It also does not account for the blade-to-blade, blade-to-hub, and blade-to-duct interactions. Therefore, as more blades and stages are added to the propeller system, the linearized slender-body theory method is unable to accurately predict the cascade and blockage effects created. This deficiency in the current vortex-lattice method is the motivation to implement an enhanced thickness model in an effort to better approximate the flow patterns through the system.

1.2 Background

1.2.1 Vortex-Lattice Lifting-Surface Analysis Tools

A comprehensive explanation of the vortex-lattice lifting-surface theory and methods for the design and analysis of marine propulsors is documented extensively [2], [3], [6], and [7]. Propeller Blade Design (hereafter designated *PBD-14*) developed by Kerwin[1] et al. was used for this research. In *PBD-14*, a lattice geometry of discrete vortex segments is placed along the blade mean camber surface. Control points are placed within each grid lattice. Blade thickness is represented using a linearize slender-body theory to obtain a source strength distribution at the lattice segments in a strip-wise sense. Each lattice segment has known source strength and the vorticity strength is solved for, such that the kinematic boundary condition is satisfied along the mean camber surface, namely the total velocity must be tangent to the surface at each control point. A trailing wake system is grown from the trailing edge of the blades. See Figure 1-1 for the vortex-lattice discretization of the propeller geometry.

[1] Justin E. Kerwin, Profesor of Naval Architecture, Ocean Engineering Department, MIT.

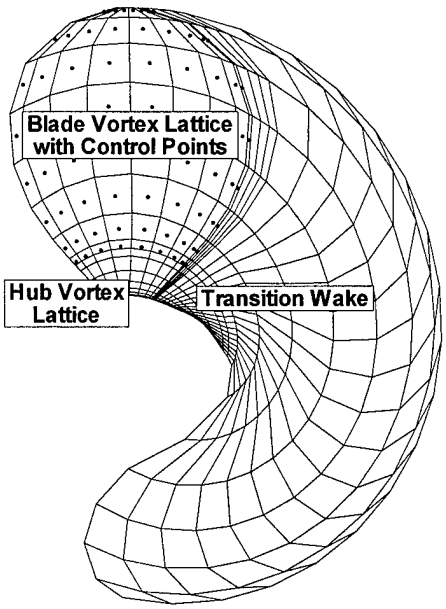

Figure 1-1: Vortex lattice discretization of a propeller geometry (4119) where the symbols represent control points.

1.2.2 Propeller Blade Thickness Modeling

It is recognized that the present method of setting the strength of the source distribution representing the blade thickness (based on linearized slender-body theory for an isolated foil) may introduce significant errors in the case of propulsors with a combination of a large thickness/chord ratio and numerous blades. The questions to be answered are:

1. Is the thickness-induced velocity correct in *PBD-14*? There are three parts to this problem:

   - isolated two-dimensional foil,
   - two-dimensional cascade effects (emulations of multi-blade flow) and
   - three-dimensional effects.

2. How does one accurately model these effects in a marine propulsor system? Two methods will be discussed below:

   - linearized slender-body theory and
   - panel method for a source distribution along the mean camber surface.

Due to efforts to more accurately assign source strengths to the vortex-lattice structure (i.e. correctly model cascade and blockage effects in propulsors), enhancements were sought in the current methodology of the source distribution to represent the blade thickness distribution. The current version of *PBD-14* uses linearized slender-body theory to predict the source strength necessary to satisfy a pseudo kinematic boundary condition at the designated control points. Regardless of the blade geometry, the kinematic boundary condition is invoked for flow over a thickened foil, assuming zero camber and loading. It performs a systematic assignment of source strengths, one chordwise strip at a time using equations 1.1 and 1.2:

$$\sigma_L = \int_{x_1}^{x_2} \sigma dx = \mathbf{V}_{total} \int_{x_1}^{x_2} \frac{\delta t}{dx} dx \tag{1.1}$$

which simplifies to

$$\sigma_L = \mathbf{V}_{total} \delta t \tag{1.2}$$

where

σ $\equiv$ the source strength distribution

σ_L $\equiv$ the source strength distribution per unit length

$\mathbf{V}_{total}$ $\equiv$ the total inflow velocity in the presence of an operating propeller

δt $\equiv$ the increase in blade thickness between lattice control points along a given chordwise strip

dx $\equiv$ the axial distance between control points being compared to determine the source strength

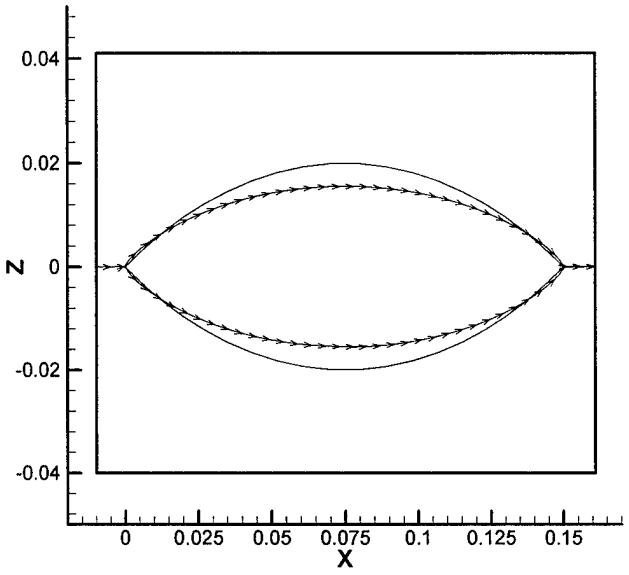

Figure 1-2: Comparison of desired thickness form and source-induced thickness form of a Biconvex blade section obtained by streamline tracing for current *PBD-14* code.

Therefore, the strength of each source line is determined using the relationship between the total inflow velocity and the differential thickness of the blade at some position (x) downstream from the leading edge of the blade section. Figure 1-2 shows an extreme test case for an infinite pitch stator in uniform flow with zero circulation (Γ) and a thickness/chord ratio of 27 percent. The desired thickness form (solid line) can be compared with the actual thickness form (vector symbols) obtained by streamline tracing. The source-induced thickness form of the section is about 20 percent too thin, thus indicating the source strength is too small.

Source Line Method

In this method, the source distribution is determined for the vortex-lattice structure by modeling the complete blade system (all blades, the hub, and the duct, if present). This is a vortex-lattice method which distributes the source line elements on the mean camber surface of a propeller blade. Then, the source distribution for the entire blade system is determined by satisfying the kinematic boundary condition at control points which are on the actual blade surface (pressure and suction sides). The result is a source strength per unit length at the vortex/source elements. This yields extremely accurate results for the foil shape shown in Figure 1-2, but gets

progressively inaccurate once the thickness/chord ratio falls below ten percent.

Source Panel Method

A alternative and more robust method, determines the source distribution for the complete blade grid structure by fully modeling the entire blade system (all blades, the hub, and the duct, if present) with source panels. This is a panel method which distributes the source panels on the mean camber surface of a propeller blade. Then, the source distribution for the entire blade system is determined by satisfying the kinematic boundary condition at control points which are on the actual blade surface (pressure and suction sides). The result is a source strength per unit area which can be integrated over the blade grid structure to obtain a similar lattice source strength per unit length as above. This yields extremely accurate results for the foil shape shown in Figure 1-2 for all ranges of the thickness/chord ratio.

1.2.3 Hub and Duct Modeling

The hub is represented by a similar vortex-lattice geometry which is appropriately placed using the method of images. The duct, if present, is developed in the same manner. The constant-strength source line elements in the hub and duct are ratioed from the blade source element strengths by comparing the lengths of the blade elements with their associated imaged elements in the hub and duct. Figure 1-3 shows a hub and duct representation in *PBD-14*.

1.3 Objective

This thesis provides a description of the advanced thickness modeling techniques implemented into the lifting-surface propeller blade design and analysis code *PBD14.3 [8]*. This enhancement extends the capability of current lifting-surface theory by properly accounting for thickness effects (cascading and blockage) in this model structure more completely. An overview of the process is presented first, followed by more detailed descriptions of the thickness modeling process. Finally, validation examples are presented.

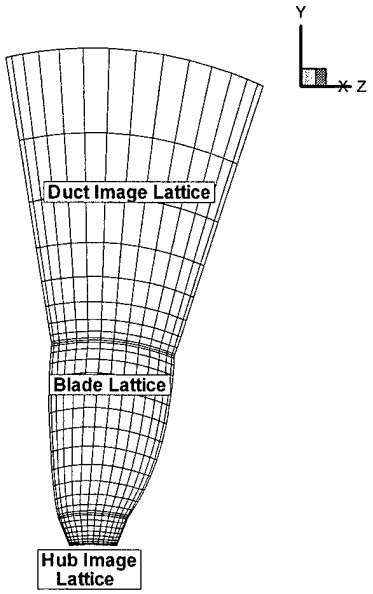

Figure 1-3: Blade, hub and duct representation in *PBD-14* for Ka-455 propulsor.

Chapter 2

Lifting-Surface Design and Analysis Theory

2.1 Overview

In the past, lifting-surface theory has provided accurate results by using slender-body theory thereby approximating higher-order thickness and higher-order viscous effects for conventional propulsors as equivalent. It has been shown that in conventional thickness and loading distributions, the decrease in lift due to viscous effects is offset by the increase in lift due to blade thickness [2]. Due to the advances in blade section design, the higher-order viscous and higher-order thickness effects do not necessarily cancel. Hence, these factors must be accounted for in the design and analysis of marine propulsors.

Lifting-surface propeller design and analysis places a vortex-lattice structure on the mean camber surface of the blade. The presence of thickness is accounted for by the distribution of sources and sink lines collocated with the vortex elements. There is a local force as a result of the velocities of a source, influencing its neighboring vortex elements. An inter-blade effect occurs due to the blockage of the modeled thickness of the blade. There is also a Lagally force that arises from the force on the sources themselves. Panel method codes model the thickness of the blade, so these effects are addressed. However, current lifting-surface codes do not have this ability [3] [9]. Also, blade thickness results in a blockage to the axisymmetric flow which affects the flow distribution past the propulsor and duct, if present. This factor must also be

taken into consideration if propulsor performance is to be predicted more accurately [10].

2.2 Vortex-Lattice Method

The vortex-lattice method of solving the lifting-surface propeller blade problem can be categorized into four separate steps:

1. A continuous vortex/source sheet, located on the blade's mean camber surface, is linearly represented by a discretized geometry for the propeller blade.

2. Determine the influence coefficients for the vortex/source distributions.

3. Apply the kinematic boundary condition which stipulates that the flow on the blade surface is only in the tangential direction.

4. Solve the system of linear equations developed from the steps outlined above.

2.2.1 Geometry Discretization

Numerically, circulation and thickness distributions are discretized using a lattice structure of constant-strength, straight-line vortex/source elements that are aligned in the chordwise and spanwise directions. These vortex/source elements are collocated along the blade's mean camber surface. *PBD-14* uses a vortex-lattice technique which incorporates a uniform B-spline representation of the blade's mean camber surface [2]. This representation of the blade allows for efficient interrogation of the B-spline control polygon to discretize the blade's surface [6]. Furthermore, various lattice structure spacing options as available (i.e. cosine and/uniform spacing) as described by Greeley and Kerwin [3]. Kelvin's Theorem states that vortex lines cannot end anywhere in the flow field, therefore trailing vortices convect downstream. The bound element with its associated convected trailers form a horseshoe vortex which extends beyond the trailing edge of the propeller blade [3]. The trailing vortices must be aligned with the flow in order to be force-free.

2.2.2 Influence Coefficients

Lifting-surface methodology solves the propulsor problem by first developing an influence matrix, $[\mathbf{HIF}_{i,j}]$. This matrix uses the induced velocity produced by each vortex/source-lattice segment as the influence (assumed unit strength of one) upon each of the blade control points. Therefore, the influence coefficients depend solely on the geometry. When this influence matrix is multiplied by the actual vortex segment strength, the induced velocity at every control point is known. Section 2.2.4 more fully explains the influence coefficients purpose in the lifting-surface methodology.

2.2.3 Kinematic Boundary Condition

In order to correctly describe the flow through the propeller blade system, one must implement the appropriate boundary condition on the rigid body. The kinematic boundary condition stipulates that no flow will penetrate the surface of the blade (i.e. the total velocity flow is tangential at the surface). Another way of stating the kinematic boundary condition is that the total velocity normal to the grid surface must be zero. This condition is specified at a number of control points on the mean camber surface which is equal to the number of vortex/source elements representing the blade lattice structure and is shown in equation 2.1 below:

$$\mathbf{V}_{total} \cdot \hat{\mathbf{n}} = 0. \tag{2.1}$$

Section 2.2.4 more fully explains how the kinematic boundary condition is utilized to solve the lifting-surface problem.

2.2.4 Solution Procedure

The lifting surface can be defined by a curvilinear system of coordinates (s_1, s_2) on the blade surface as shown in Figure 2-1. The surface coordinates are defined as

$$\mathbf{x}(s_1, s_2) = [x(s_1, s_2), y(s_1, s_2), z(s_1, s_2)] \tag{2.2}$$

and the metric coefficients are given as

$$h_1 = \left| \frac{\partial \mathbf{x}}{\partial s_1} \right| \tag{2.3}$$

and

$$h_2 = \left| \frac{\partial \mathbf{x}}{\partial s_2} \right|. \tag{2.4}$$

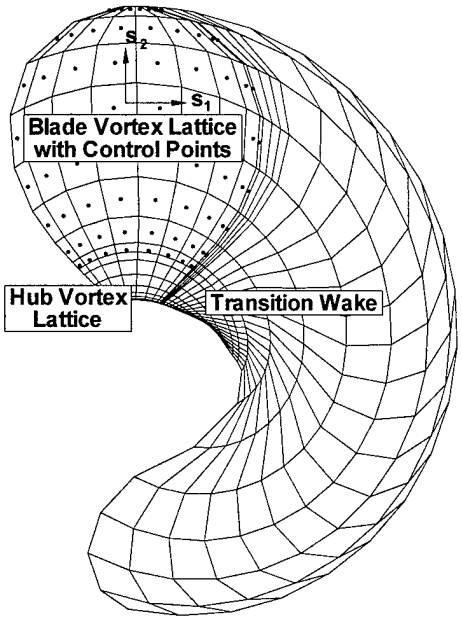

Figure 2-1: Vortex lattice discretization of a propeller geometry where the symbols represent control points and s_1 and s_2 are orthogonal vectors on the blade surface.

The kinematic boundary condition is given as

$$\int_{\mathbf{S}+\mathbf{S_w}} \frac{[\gamma(s_1', s_2') \times \mathbf{R}] \cdot \hat{\mathbf{n}}}{4\pi R^3} h_1 h_2 ds_1' ds_2' = -[U_{in}(s_1, s_2) + \Omega R + V_{ind}(s_1, s_2)] \cdot \hat{\mathbf{n}} \tag{2.5}$$

where

$$\mathbf{R} \equiv \mathbf{x}(s_1, s_2) - \mathbf{x}(s_1', s_2')$$

$$\hat{\mathbf{n}} \equiv \text{vector normal to S at point } (s_1, s_2).$$

Equation 2.5 specifies that there is no flow through the blade surface S, considering a continuous sheet of vorticity (γ) on the blade surface and in the wake (S_w) in the presence of an incoming flow (U_{in}) and rotational velocity (ΩR). Since the thickness distribution for the blade is known, the source-induced velocities ($V_{ind_{total}}$) may be computed and included on the right hand side of the equation [10].

A lifting-surface code is used for either a design of a new propulsor or an analysis of an existing propulsor. In each case, equation 2.5 applies, but the known versus unknowns vary. For propulsor design, a desired radial and chordwise loading distribution is prescribed. Then, the blade shape is manipulated until equation 2.5 is satisfied. For propulsor analysis, the blade shape is prescribed. Then, the resulting circulation is solved. This process summation is simplified to matrix equation 2.6:

$$[\mathbf{HIF}_{i,j}] \cdot [\Gamma_j] = -[\mathbf{V}_j \cdot \hat{\mathbf{n}}] \tag{2.6}$$

where

$\mathbf{HIF}_{i,j} \equiv$ matrix of horseshoe influence coefficients. The subscripts denote the influence of the j^{th} horseshoe vortex on the i^{th} control point. Each element represents the velocity component normal to S, induced at a control point due to a horseshoe vortex of unit strength.

$\mathbf{\Gamma}_j \equiv$ blade circulation scalar composed of individual vortex strengths of the j^{th} vortex.

$\mathbf{V}_j \cdot \hat{\mathbf{n}} \equiv$ velocity component normal to the blade mean camber surface at the i^{th} control point.

Solving this matrix system of linear equations yields equation 2.7:

$$[\Gamma_j] = -[\mathbf{V}_j \cdot \hat{\mathbf{n}}][\mathbf{HIF}_{i,j}]^{-1} \tag{2.7}$$

Blade thickness effects are added by placing discrete source lines coincident with the chordwise blade vortex elements. The resulting propulsor forces due to the lifting surface and thickness are calculated from the Kutta-Joukowski and Lagally theorems, respectively. A leading edge suction force and Lighthill pressure distribution correction are applied to those forces, and the propulsor's sectional viscous drag is calculated based on either stripwise two-dimensional empirical drag coefficients or a stripwise two-dimensional integral boundary layer calculation.

2.3 Propulsor Inflow

The accuracy of modeling the propulsor is dependent upon correctly representing the propeller inflow. The three concepts for propeller inflow are:

Definition 1 *Nominal inflow: Velocity field at the plane of the propeller when the propeller is not operating.*

Definition 2 *Total inflow: Velocity field at the plane of the propeller when the propeller is operating.*

Definition 3 *Effective inflow: Total inflow without the effects of the propeller induced velocities.*

In propeller design and analysis, the lifting-surface methodology deals with the flow resulting from the operation of the propeller in a specified axisymmetric effective inflow. Therefore, the total velocity relation at the blade surface in the axial, radial and tangential directions can be decomposed into the following three components

$$\mathbf{V}_{total} = \mathbf{V}_{eff} + \overline{\mathbf{V}}_{ind_{cmv}} + \widetilde{\mathbf{V}}_{ind_{fluc}} \tag{2.8}$$

where

$\mathbf{V}_{total}$ $\equiv$ the total velocity in the presence of an operating propeller at a given point on the blade.

$\mathbf{V}_{eff}$ $\equiv$ the effective wake behind the ship.

$\overline{\mathbf{V}}_{ind_{cmv}}$ $\equiv$ the circumferential mean velocity induced due to propeller blades and wakes.

$\widetilde{\mathbf{V}}_{ind_{fluc}}$ $\equiv$ the fluctuating component of induced velocity due to propeller blades.

Therefore, the total velocity is a combination of the effective inflow and the net propeller blade induced velocities. In the propeller blade problem, the total velocity is used to solve the kinematic boundary condition as shown in equation 2.1.

Chapter 3

Numerical Implementation of the Enhanced Blade Thickness Model

3.1 Overview

In the current version of *PBD-14*, propeller lifting-surface design and analysis program code, the thickness distribution is developed in the following manner using linearized slender-body theory:

1. For a chordwise strip, determine the thickness distribution from the B-splined input file parameters and the change in thickness (δt) between the vortex-lattice structure control points (dx).

2. Use the flow field's circumferential mean velocity (CMV) and rotational velocity component (ΩR) to determine the blade's local velocity at the control points (along the mean camber surface).

3. Solve for the source/sink line elements constant-strength ($\sigma_{Li,j}$) necessary to create the correct δt between the control points on that spanwise strip. Equation 3.1 shows that the source strength per unit length is a function of inflow velocity, the change in the thickness distribution and the differential length between control points:

$$\sigma_{Li,j} = \mathbf{V}_{total}\delta t. \tag{3.1}$$

4. Adjust each source line element strength for "slant." This effect increases the strength of the source line element when it is not perpendicularly aligned with the inflow by a factor of $\frac{L_{total}}{dR}$. Here, L_{total} is the total length of the element and dR is the radial difference between element endpoints.

5. Correct the sink strengths to ensure each chordwise strip of source/sink line elements sums to zero. This effect increases each sink element strength by a factor of $\frac{\sigma_{src}}{\sigma_{snk}}$, thus ensuring that the $\sum \sigma_{src} + \sum \sigma_{snk} = 0$.

This methodology was flawed for cases where the blade design had numerous blades and/or a high thickness/chord ratio ($\geq$ 10%). This scheme did not account for blade-on-blade, hub-on-blade, or duct-on-blade effects in the source line strength determination. Therefore, as the source lines of each modeled propeller section and its associated components get closer together, these effects increase in importance (i.e. far field effects begin to move into the near field range to increase the influence of these elements on one another).

Because of the shortcomings of this methodology, more accurate methods of accounting for blade, hub and duct interactions to more fully represent the propulsor were investigated. Two promising techniques were developed, implemented and tested in *PBD-14*:

1. Source Line Method

2. Source Panel Method.

The source panel method is an improvement upon the work completed in the source line method. This work was undertaken to develop a more robust representation of all the effects that determine the blade thickness distribution. For example, the source line method accounted for the cascade effect (increasing the number of blades creates larger blade-to-blade influences). It also was able to properly represent the blade thickness distribution for large thickness/chord ratios. Both of these efforts were improvements over the shortcomings of the previous *PBD-14* methodology of assigning source strengths. However, the source line method over predicted the blade thickness distribution when the thickness/chord ratio decreased to less than ten percent. This effect got worse as the thickness/chord ratio decreased. The source panel method corrects the shortcomings of the source line method, so that it accurately represents the blade thickness distribution over the broadest range of thickness/chord ratios and numbers of blades.

3.2 Source Line Method

This thesis seeks to find improvements in *PBD-14* to more accurately represent the blade thickness distribution over the blade lattice structure in the presence of numerous blades or large thickness/chord ratios led to the development of the source line methodology. An outline of this method follows:

1. Discretize the blade geometry on the mean camber surface so that the vortex and source elements are collocated.

2. Develop each chordwise blade thickness distribution from the PBD-14 input file $\frac{t}{D}$ values shown in Appendix B.

3. Fully develop the blade's actual outer surface for each spanwise position at each vortex element endpoint that lies on the mean camber surface. This is accomplished by creating the pressure and suction side surfaces from the actual thickness distribution of the blade section at the mean the camber surface vortex/source elements. The mean camber surface lattice endpoints were moved in the normal direction by the appropriate δt for the specified point. Figures 3-1 and 3-2 show the discretized geometry of a propeller blade with the pressure and suction side surfaces included.

4. Develop a complete set of control points and a normal to the control points on the pressure and suction side of the actual blade surface. This is done in the same fashion as the mean camber surface calculations in previous versions of *PBD-14*.

5. Develop the hub and duct imaged lattice structure. The hub and duct images lie along the mean camber surface of the inner and outermost spanwise set of endpoints, thus having the same pitch of the blade at the hub and duct intersection points. Also, the hub and duct imaged source strengths are adjusted by a factor of $\frac{L_{bldelem}}{L_{hubelem}}$ and $\frac{L_{bldelem}}{L_{ductelem}}$, respectively.

6. Determine the total inflow velocity at the control points on the blade's mean camber surface.

7. Develop a system of linear equations in matrix form, similar to equation 2.6, to solve for the source strengths associated with each of the source-induced function coefficients $[\mathbf{SIF}_{i,j}]$. This is done while satisfying the kinematic boundary condition ($\mathbf{V}_{total} \cdot \hat{\mathbf{n}} = 0$) at the control points on the actual pressure and suction side surfaces of the blade. The set of matrix equations is increased to add a further condition that the $\sum \sigma_{src} + \sum \sigma_{snk} = 0$ for each chordwise strip on the blade.

This set of matrix equations is shown in a simplified notation in equation 3.2:

$$[\mathbf{SIF}_{i,j}] \cdot [\sigma_{L_j}] = -[\mathbf{V}_j \cdot \hat{\mathbf{n}}] \tag{3.2}$$

where

$\mathbf{SIF}_{i,j}$ $\equiv$ matrix of source influence coefficients. The subscripts denote the influence of the j^{th} source element on the i^{th} control point. Each element represents the velocity component normal to S, induced at a control point due to a source element of unit strength.

$\boldsymbol{\sigma}_{L_j}$ $\equiv$ constant strength source composed of individual source strengths of the j^{th} source elemnts.

$\mathbf{V}_j \cdot \hat{\mathbf{n}}$ $\equiv$ velocity component normal to the blade mean camber surface at the i^{th} control point.

Solving this matrix system of linear equations yields equation 3.3

$$[\sigma_{L_j}] = -[\mathbf{V}_j \cdot \hat{\mathbf{n}}][\mathbf{SIF}_{i,j}]^{-1}. \tag{3.3}$$

In order to determine what truly affects the blade thickness distribution problem, a decomposition of source and vortex velocities at the pressure, suction and mean camber surfaces was necessary. Figure 3-3 shows a simple chordwise blade representation for the velocity effects on the blade thickness distribution. The proof follows.

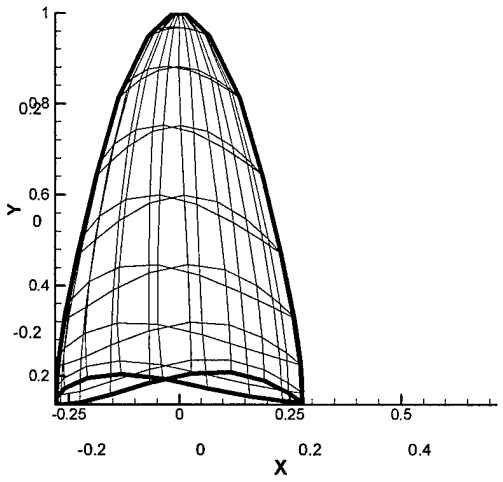

Figure 3-1: XY-coordinates for blade thickness discretization on the pressure and suction sides.

Definitions for the nomenclature in Figure 3-3 is:

$-$ $\equiv$ pressure surface (lower) of the blade.

$+$ $\equiv$ suction surface (upper) of the blade.

m $\equiv$ mean camber surface (middle) of the blade.

$\hat{\mathbf{n}}$ $\equiv$ normal for pressure and suction side surfaces.

$\hat{\mathbf{t}}$ $\equiv$ tangent for pressure and suction side surfaces.

(s_1, s_2) $\equiv$ local coordinates in normal (1) and tangential (2) directions on the mean camber surface.

(U_{s_1}, U_{s_2}) $\equiv$ component of inflow velocity in the normal (1) and tangential (2) directions.

$(V\sigma_{s_1}, V\sigma_{s_2})$ $\equiv$ component of velocity due to sources.

$(V\gamma_{s_1}, V\gamma_{s_2})$ $\equiv$ component of velocity due to vortices.

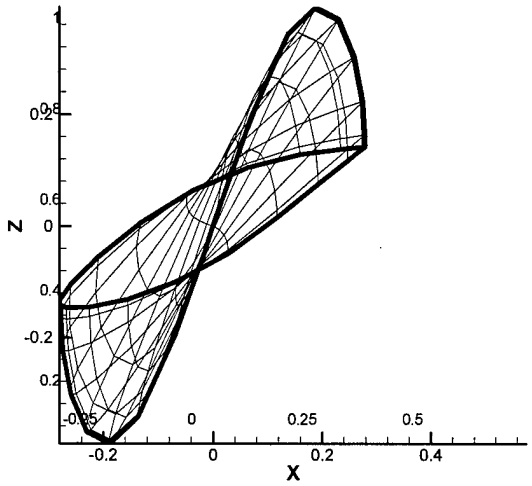

Figure 3-2: XZ-coordinates for blade thickness discretization on the pressure and suction sides.

In order to meet the kinematic boundary condition on both the pressure and suction side surfaces of the blade, equations 3.4 and 3.5 must hold true.

$$\left[\left(U_{s_1} + V\sigma_{s_1} + V\gamma_{s_1}\right)\hat{\mathbf{n}} + \left(U_{s_2} + V\sigma_{s_2} + V\gamma_{s_2}\right)\hat{\mathbf{t}}\right]_+ = 0 \tag{3.4}$$

$$\left[\left(U_{s_1} + V\sigma_{s_1} + V\gamma_{s_1}\right)\hat{\mathbf{n}} + \left(U_{s_2} + V\sigma_{s_2} + V\gamma_{s_2}\right)\hat{\mathbf{t}}\right]_- = 0 \tag{3.5}$$

where

$$\hat{\mathbf{n}}_+ = -\hat{\mathbf{n}}_- \text{ and } \hat{\mathbf{t}}_+ = \hat{\mathbf{t}}_- \text{ exactly,}$$

and for small thickness distributions,

$$V\gamma_{s_{1+}} \approx V\gamma_{s_{1-}}.$$

From substitution and adding equations 3.4 and 3.5, the following result is obtained

$$\frac{\left(V\sigma_{s_{1+}} - V\sigma_{s_{1-}}\right)}{2}\hat{\mathbf{n}}_+ + \left[U_{s_2} + \frac{\left(V\sigma_{s_{2+}} + V\sigma_{s_{2-}}\right)}{2} + \frac{\left(V\gamma_{s_{2+}} + V\gamma_{s_{2-}}\right)}{2}\right]\hat{\mathbf{t}}_- = 0. \tag{3.6}$$

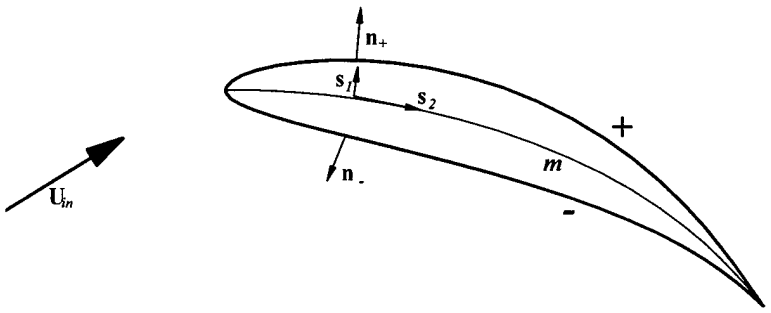

Figure 3-3: Chordwise strip of a blade section to represent the components which affect blade thickness distribution.

Assuming a small thickness distribution, Figure 3-4 shows a simplified mean camber line representation of $V\gamma_{s_2}$.

Since $V\gamma_{s_{2,u}} = V\gamma_{s_{2,m}} + \frac{\gamma}{2}$ and $V\gamma_{s_{2,\ell}} = V\gamma_{s_{2,m}} - \frac{\gamma}{2}$, then averaging the effects of the vortex induced velocities from the pressure and suction surfaces of the blade at the mean camber surface produces $V\gamma_{s_2} = \frac{\left(V\gamma_{s_{2+}} + V\gamma_{-}\right)}{2} = V\gamma_{s_{2,m}}$. Hence, equation 3.6 can be simplified further

$$\frac{(V\sigma_{s_{1+}} - V\sigma_{s_{1-}})}{2}\hat{\mathbf{n}}_+ + \left[U_{s_2} + \frac{(V\sigma_{s_{2+}} + V\sigma_{s_{2-}})}{2} + V\gamma_{s_2}\right]\hat{\mathbf{t}}_+ = 0. \tag{3.7}$$

Furthermore, for a symmetric, two dimensional foil, $V\gamma_{s_2} = 0$. Also, if the foil has a moderate camber, like most propeller blade sections, $V\gamma_{s_2} \approx 0$ and can be considered as a part of the CMV inflow. This assumes that $V\gamma_{s_2}$ is a small percentage of total CMV inflow which is made up of many components. Therefore, the $V\gamma_{s_2}$ component of velocity can be moved to the right

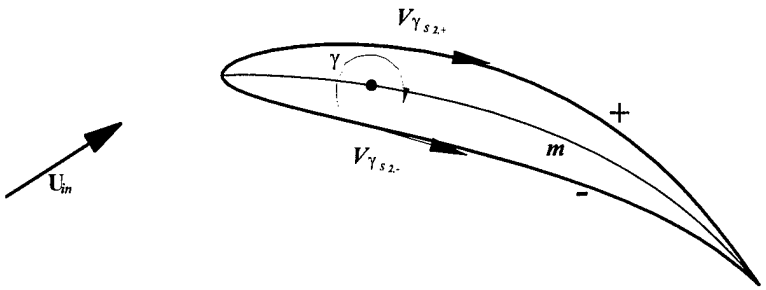

Figure 3-4: Mean camber line representation of vortex-induced velocities averaging to $V\gamma_{s_2}$.

hand side of equation 2.6 and iterated upon to get a final solution.

Finally, $V\sigma_{s_{1+}}$ and $V\sigma_{s_{1-}}$ on the pressure and suction side surfaces of the blade can be expressed as a dot product of the source-induced influence coefficients $[\mathbf{SIF}_{i,j}]$ and the unknown source line strength $[\sigma_{L_j}]$. Thus, equation 3.7 simplifies to the matrix equation 3.2.

To check this reasoning, a symmetrical, two-dimensional foil is placed at an arbitrary angle of attack (α) as shown in Figure 3-5. Since $U_{s_{1+}} = U_{in}\sin\alpha$, $U_{s_{1-}} = U_{in}\sin\alpha$ and $U_{s_{2+}} = U_{s_{2-}} = U_{in}\cos\alpha$, then substituting these parameters into equation 3.7, yields the expected result that the blade thickness distribution is only affected by $U_{in}\cos\alpha$ or

$$V\sigma_{s_1}\hat{\mathbf{n}}_+ + (U_{in}\cos\alpha + V\sigma_{s_2})\,\hat{\mathbf{t}}_+ = 0. \tag{3.8}$$

Once source-induced coefficients are developed for the pressure and suction side surfaces of the blade, they are averaged to get a representative $[\mathbf{SIF}_{i,j}]$ coefficient matrix for the mean

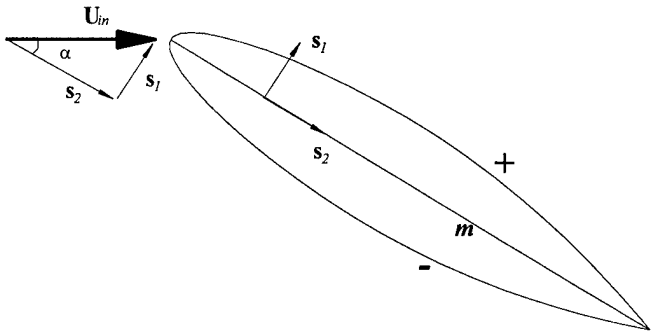

Figure 3-5: Two-dimensional blade section used to check what attributes affect blade thickness distribution.

camber surface. The mathematical formulation is solved using a least squares methodology which already existed in the *PBD-14* code. In this solution formulation, the hub-to-blade and duct-to-blade imaged influence coefficients are added directly to the blade-to-blade influence coefficients. This is explained more fully in Section 3.4.2. This is a more robust and accurate method than the current *PBD-14* code since the kinematic boundary condition is satisfied on the actual blade surface at the new set of control points developed on this surface.

3.3 Source Panel Method

A second method to accurately model the source distributions over the blade's mean camber surface was developed after the shortcomings of the source line method were found. While the source line method accurately represents propulsors with numerous blades and large thick-

ness/chord ratios, it fails to correctly represent thinner blades where the thickness/chord ratio approaches zero. In fact, it begins to over predict the source line strengths and hence the blade thickness distribution when the thickness/chord ratio becomes less than about ten percent.

Because source line elements are a set of discrete concentrations of constant-strength sources, they tend to average the effects between control point positions, where the kinematic boundary condition is invoked for equation 3.9. This becomes more difficult for the system of linear equations as the blade thickness distribution approaches zero (i.e. matrix equation 3.2 becomes ill-conditioned and obtaining a solution by the least squares method is impossible). Therefore, the next logical step to obtain a less discrete concentration of the constant strength source distributions, but still accurately represent the blade thickness distribution is to move from line sources (σ_L) to area sources (σ_A) or panels. This source panel methodology seeks to obtain results with the same accuracy as the source line method at large thickness/chord ratios and numerous blades. However, it also seeks to improve upon the linearized slender-body theory approximation results of the current *PBD-14* code as thickness/chord ratio approaches zero. This source panel method is outlined below:

1. Discretize the entire B-spline blade geometry on the mean camber surface, to include both the leading and trailing edges. This means that one extra control point must be created at the leading edge.

2. Develop each chordwise blade thickness distribution from the PBD-14 input file $\frac{t}{D}$ values shown in Appendix B.

3. Fully develop the blade's actual outer surface for each spanwise position at each vortex element endpoint that lies on the mean camber surface. This is accomplished by creating the pressure and suction side surfaces from the actual thickness distribution of the blade section at the mean the camber surface vortex/source elements. The mean camber surface lattice endpoints were moved in the normal direction by the appropriate δt for the specified point. Figures 3-1 and 3-2 show the discretized geometry of a propeller blade with the pressure and suction side surfaces included.

4. Develop a complete set of control points and a normal to the control points on the pressure and suction side of the actual blade surface. This is done in the same fashion as the mean

camber surface calculations in previous versions of *PBD-14*. However, the leading and trailing edge control points are moved off the actual edge of the mean camber surface to a position between the lattice structure elements.

5. Develop the hub and duct imaged panel structure. The hub and duct images lie along the mean camber surface of the inner and outermost spanwise set of endpoints, thus having the same pitch of the blade at the hub and duct intersection points. However, the hub and duct imaged source strengths no longer require an adjustment by a factor of $\frac{L_{bldelem}}{L_{hubelem}}$ and $\frac{L_{bldelem}}{L_{ductelem}}$ respectively. This is due to the robust nature of the panel methodology imposed with this technique.

6. Determine the total inflow velocity at the control points on the blade's mean camber surface.

7. Develop a system of linear equations in matrix form, similar to equation 3.2, to solve for the source strengths associated with each of the source-induced function coefficients $[\mathbf{SIF}_{i,j}]$. This is done while satisfying the kinematic boundary condition $(\mathbf{V}_{total} \cdot \hat{\mathbf{n}} = 0)$ at the control points on the actual pressure and suction side surfaces of the blade. The set of matrix equations is increased to add a further condition that the $\sum A_{src} + \sum A_{snk} = 0$ for each chordwise strip.

This set of matrix equations is shown in a simplified notation in equation 3.9:

$$[\mathbf{SIF}_{i,j}] \cdot [\sigma_{A_j}] = -[\mathbf{V}_j \cdot \hat{\mathbf{n}}]. \tag{3.9}$$

Similar to the reasoning discussed in Section 3.2, the same conclusions can be drawn about the velocity contributions to the blade thickness distribution. The following section will cover the modifications required to the *PBD-14* code to implement this methodology.

New influence function subroutines have to be coded with the equations found in Appendix A. In the three-dimensional case, the discretization has two parts:

- discretize the geometry
- determine the singularity element distribution.

If these elements are represented by a B-spline net, both geometry and singularity strength, then the first order approximation to the surface can be defined as a quadrilateral panel[1] with a constant-strength source singularity. Since a vortex-lattice mean camber surface is represented as a lattice structure of rectilinear panels,[2] a conversion from a rectilinear surface to a quadrilateral surface is performed [11]. From Appendix A, the potential at an arbitrary point $P(x,y,z)$ due to this quadrilateral element is

$$\Phi(x,y,z) = -\frac{\sigma_A}{4\pi}\int_S \frac{dS}{\sqrt{(x-x_0)^2+(y-y_0)^2+(z-z_0)^2}} \tag{3.10}$$

and the velocity components can be obtained by differentiating the velocity potential:

$$(u,v,w) = (\frac{\partial\Phi}{\partial x}, \frac{\partial\Phi}{\partial y}, \frac{\partial\Phi}{\partial z}). \tag{3.11}$$

This differentiation from equation 3.11 results in source-induced velocity coefficients used to obtain blade-to-blade, hub-to-blade, and duct-to-blade influence functions.

3.4 Integration of the Source Panel Model in *PBD-14*

3.4.1 Blade Lattice Modification

The current methodology uses a vortex-lattice structure which does not include the actual leading edge section (B-spline leading edge endpoints to the first vortex/source element). The new methodology is to use the entire cubic B-spline blade structure, leading edge to trailing edge, to describe the source distribution lines. This allowed for a symmetric distribution of source panels for cosine spacing in the chordwise direction along the mean camber surface. However, the number of source panels increases by one more than vortex elements. Control points were placed as before with two exceptions:

1. a leading edge control point was added and placed in a similar fashion as the other control points (about the middle of the lattice rectilinear panel); and

[1] A quadrilateral panel is a flat surface with four straight sides.
[2] A rectilinear panel has straight but not necessarily flat sides that can be twisted.

2. the trailing edge control point was moved and placed in a similar fashion of the other control points, vice right on the trailing edge.

These two exceptions were necessary so that the control points did not lie on the edge of a source panel and create a singularity for the system of linear equations, thus forming an ill-conditioned matrix. Similarly, the hub and duct images were developed from source panels vice source line elements.

To further enhance the model and truly satisfy the kinematic boundary condition, the lattice points for the entire mean camber surface were moved to both the pressure and suction side surfaces of the blade. From these new surfaces, control points were added in the same fashion as the current *PBD-14* code did on the mean camber surface. Figures 3-1 and 3-2 show the fully developed blade lattice structure.

Lastly, the rectilinear panels which form the entire mean camber surface set of source panels had to be transformed into quadrilateral panels which approximate the same constant-strength source distribution. This transformation was completed so that the code in reference [11], which solves for σ_A, could be utilized. This transformation was accomplished using a set of subroutines for *PSF10.3* code. These subroutines input the rectilinear panel ends consisting of four endpoint coordinates. Then, the subroutines return the quadrilateral panel endpoints which lie on a constant $z - plane$ and a set of coordinates for the actual center of the original rectilinear panel. Therefore, the orientation between the local and global coordinate system is maintained.

3.4.2 Adjustments to the Solution Procedure

The solution procedure for constant-strength source area distribution is completely different from the current *PBD-14* code. It now accounts for blade-to-blade, hub-to-blade and duct-to-blade influence interactions which affects induced velocities produced within the propulsor. These new influence coefficients are the averaged values of the pressure and suction side $[\mathbf{SIF}_{i,j}]$ matrix which represents the mean camber surface $[\mathbf{SIF}_{i,j}]$ matrix. The solution is solved as a system of linear equations via a least squares method vice a strict, two-dimensional, linearized, slender-body theory. By incorporating the effects of the other blades, the hub and the duct, if present, the model more accurately represents cascade and blockage effects which affect the

blade thickness distribution. Therefore, the propulsor blade representation is more accurate in a larger variety of propulsor types.

Since panels are now utilized to obtain the constant-strength source distributions, there is a discrepancy in how *PBD-14* must account for this source distribution. One method is to integrate the source panel strengths in the chordwise direction. This integration technique would lump the effects of the panels into source line elements which are collocated with the vortex elements. While this method is still an improvement over the source line method and linearized slender-body theory, it still diminishes the robust nature of the method.

Therefore, a separate velocity matrix was developed from the new known source strength distribution for the blade, hub and duct interactions at the old control point positions on the mean camber surface.

$$[\mathbf{V}_{ind_j} \cdot \hat{\mathbf{n}}] = -[\mathbf{SIF}_{i,j}] \cdot [\sigma_{A_j}]. \tag{3.12}$$

Equation 3.12 shows the velocity matrix that will be imported into the $[\mathbf{HIF}_{i,j}]$ system of linear equations, as a known velocity vector of source-induced effects on the right-hand side of the equation. This velocity vector will be calculated using the source panel influences on the specified control points vice the source line element influences. Then, this modified version of the $[\mathbf{HIF}_{i,j}]$ system of equations will be solved to obtain $[\mathbf{\Gamma}_j]$.

3.4.3 Adjustments to Hub and Duct Modeling

The method of images is used in *PBD-14* to represent the hub and duct. This provides a means to implement boundary conditions necessary in potential flow theory. For singularities on rigid boundaries, potential flow introduces another singularity into the flow field which mirrors the original singularity. The vortex element images model the hub and duct accurately and are satisfactory from the standpoint of meeting the kinematic boundary condition. However, the source element images are less accurate. The resulting imaged-lattice structure is exhibited in Figure 1-3. The imaged source panels for the hub and duct are created in the same manner as the blade source panels.

Role of the Hub and Duct

Adding the hub and duct source influence functions to the $[\mathbf{SIF}_{i,j}]$ matrix system expands the complexity of appropriately accounting the influences on each control point, but does not complicate the actual system of linear equations that must be solved. Equation 3.13 presents the expanded influence function coefficient for a generalized control point position:

$$\begin{array}{l} \\ Control \\ \\ Points \end{array} \begin{array}{c} \begin{array}{c} Source \quad Panels \end{array} \\ \left[\begin{array}{c} \mathbf{SIF_{BB}}_{i,j} + \mathbf{SIF_{HB}}_{i,j} + \mathbf{SIF_{DB}}_{i,j} \quad \Longrightarrow \\ \\ \Downarrow \end{array} \right] \end{array} \cdot [\sigma_{A_j}] = -[\mathbf{V}_j \cdot \hat{\mathbf{n}}]. \tag{3.13}$$

The above equation appears complex, however, it is merely an extension of the blade-only formulation (see equation 3.9).

Hub and duct surfaces at the blade endpoints are streamlines of the flow, where the component of $\mathbf{V}_{total}$ normal to the blade surface is zero. The hub and duct source panel influences on the blade vortex-lattice system induces zero CMV normal to the blade surface. This has been exhibited by a field-point velocity calculation routine at the control points on the blade surface [6], as well as by the velocity streamline traces developed in the next chapter.

Chapter 4

Validation

In this chapter, two methods of evaluating stators are compared. First, an infinite-pitch, constant $\frac{t}{D}$ stator with a hub and duct in a uniform inflow is evaluated. The original *PBD-14* scheme will be compared to the source panel method for a variety of thickness distributions at different angles of attack to exhibit the differences in how each method represents of source-induced effects. Second, an infinite-pitch, constant $\frac{t}{D}$ stator in a uniform inflow is evaluated at the hub and duct to ensure their effects are accounted for properly. Finally, the number of blades will be increased to eleven and the effects analyzed at the hub. Since the most significant source-induced factors occur at this point, then cascade effect analysis will be performed here. The source panel method will exhibit its robustness when it uses varying blade thickness distributions for two different blade section geometries.

4.1 The Infinite-Pitch, Constant $\frac{t}{D}$ Stator

This test case shows that the source panel method is more robust than the linearized slender-body theory of the original *PBD-14* code for a larger range of thickness/chord ratios and number of blades. Results vary with vortex-lattice grid density and therefore all comparisons will be made with a 15 x 15 grid. Table 4.1 shows how the parameters for the stator will be varied in this test case.

Blade Section Shape	Angle of Attack (α)	t/D	thickness/chord
NACA66 modified	0°	0.020	26.67%
Biconvex	1°	0.015	20.00%
	5°	0.010	13.33%
		0.002	2.67%

Table 4.1: Infinite-pitch, constant t/D stator parameters

x	y	z	R
0.00	0.20	0.00	0.20
0.05	0.50	0.00	0.50
0.10	0.80	0.00	0.80
0.15	1.00	0.00	1.00

Table 4.2: Infinite-pitch, constant t/D stator with a zero degree angle of attack.

4.1.1 Initial Comparison for Large $\frac{t}{D}$ Values at a Zero Angle of Attack

Comparison of current *PBD-14* and source panel method for the blade section shapes listed in Table 4.1 is exhibited in Figures 4-1 and 4-2. This set of figures shows how the linearized slender-body theory approximations for blade thickness distribution are inadequate when the blade section becomes thicker. Figures 4-3 and 4-4 show the results for the source panel method which has less than one percent error associated with the blade thickness distribution. Because of the straightforward shape (no camber, as seen in Table 4.2) and uniform inflow, this set of stators does not produce any circulation or forces which was verified by the PBDOUT.SGR file. The blade lattice structure is a 15 X 15 grid with hub and duct images (7) implemented. The dividing streamline is shown so that the modeled thickness distribution (velocity streamlines) can be compared with the actual thickness distribution on the pressure and suction side surfaces of the blade. The cut is made midspan on the blade.

4.1.2 Comparisons at a One Degree Angle of Attack

The next step was to place the blades at an angle of attack greater than zero. This would test equation 3.8 results that predicted the tangential velocity component on the mean camber surface ($U_{in}\cos\alpha$) is the only affect the blade thickness distribution. Figures 4-5 through 4-6 exhibit the continued trend for the original *PBD-14* code to under predict the blade thickness distribution at the larger thickness/chord ratios. Also, the results of equation 3.8 are verified in

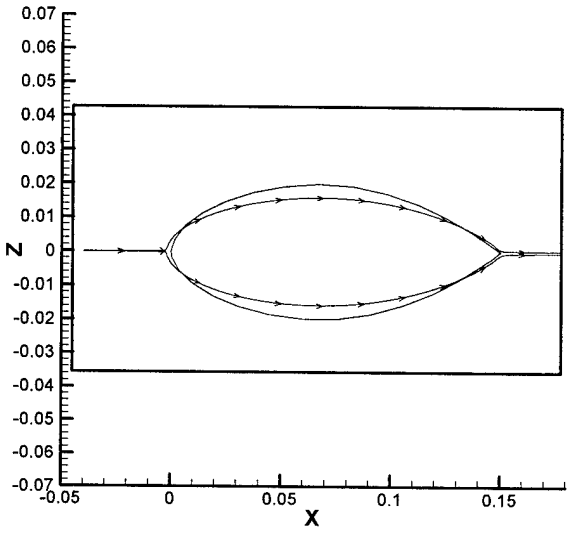

Figure 4-1: Linearized slender-body theory velocity streamline results for a NACA66 modified blade section with $\frac{t}{D} = 0.020$ and $\alpha = 0°$ in a uniform inflow.

x	y	z	R
0.00000000	0.20000000	0.00000000	0.20
0.04999239	0.19999810	0.00087262	0.50
0.09998477	0.19999239	0.00174524	0.80
0.14997715	0.19998287	0.00261786	1.00

Table 4.3: Infinite-pitch, constant t/D stator with an one degree angle of attack.

Figures 4-7 and 4-8. Because of the angle of attack (Table 4.3 shows the stator's B-spline net design for this α) and uniform inflow, this set of stators produces some circulation and forces which was verified by the PBDOUT.SGR file.

4.1.3 Comparisons at a Five Degree Angle of Attack

The next step was to place the blades at an angle of attack greater than one. This would test equation 3.8 results further. Figures 4-9 and 4-10 exhibit the continued trend for the original *PBD-14* code to under predict the blade thickness distribution at the larger thickness/chord ratios. Also, the results of equation 3.8 are well supported in Figures 4-11 and 4-12, even though the streamlines do not exactly match the actual thickness distribution shape. However, this

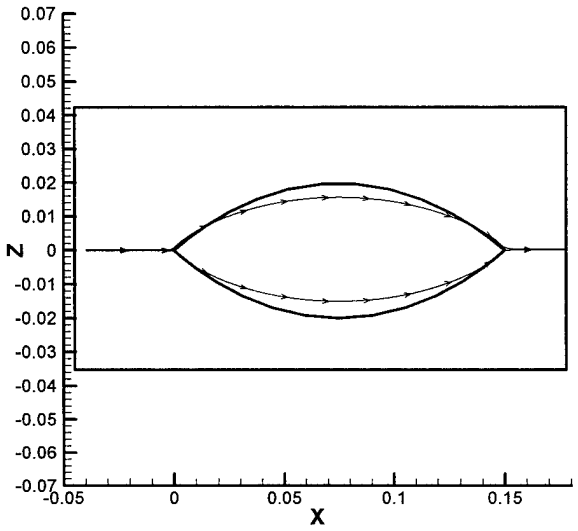

Figure 4-2: Linearized slender-body theory velocity streamline results for a Biconvex blade section with $\frac{t}{D} = 0.020$ and $\alpha = 0°$ in a uniform inflow.

x	y	z	R
0.00000000	0.20000000	0.00000000	0.20
0.04980973	0.19985742	0.00435779	0.50
0.09961947	0.19971046	0.00871557	0.80
0.14942920	0.19957226	0.01307336	1.00

Table 4.4: Infinite-pitch, constant t/D stator with a five degree angle of attack.

series of figures definitely shows the improvements that the source panel method makes to the overall blade thickness distribution representation in many different scenarios. Because of the angle of attack (Table 4.4 shows the stator's B-spline net design for this α) and uniform inflow, this set of stators produces some circulation and forces which was verified by the PBDOUT.SGR file.

4.1.4 Varying the Thickness/Chord Ratio at a Zero Angle of Attack

To show the robustness of the source panel method over the linearized slender-body theory, different thickness/chord ratios are compared in Figures 4-13 through 4-16, including the Figures 4-2 and 4-4 (thickness/chord ratio of 26.67%). As as the thickness/chord ratio approaches zero,

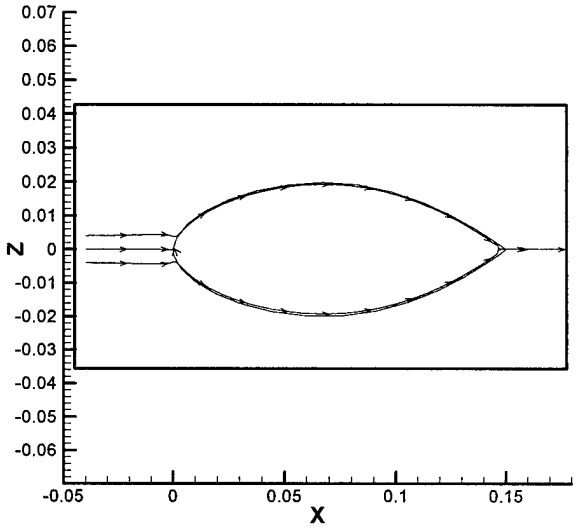

Figure 4-3: Source panel method velocity streamline results for a NACA66 modified blade section with $\frac{t}{D} = 0.020$ and $\alpha = 0°$ in a uniform inflow.

the source panel method and linearized slender-body theory begin to merge to the same blade thickness distribution, as expected. Note that as the blade thickness distribution approaches zero, it is better to increase the grid density to obtain a finer source and vortex strength distribution over the blade. In this manner, the blade representation is more accurate, but computational time increases. For some cases it may be necessary to increase the grid density to 25 x 25 or even 35 x 35.

4.1.5 Hub and Duct Interfaces and the Cascade Effect

Finally, the next example is just a check that the source panel method with hub and duct modeling yields the correct blade thickness distribution at these intersecting points on the model. Figures 4-17 and 4-18 exhibit the robustness of the source panel method to include all effects (blade-to-blade, hub-to-blade, and duct-to-blade) of the sourced-induced functions accurately. A special case of the hub interface with the blades is shown in Figure 4-19 where the number of blades increases to eleven. The source distribution increases to appropriately represent the cascade effect in the model. Note that the source panel method still exhibits

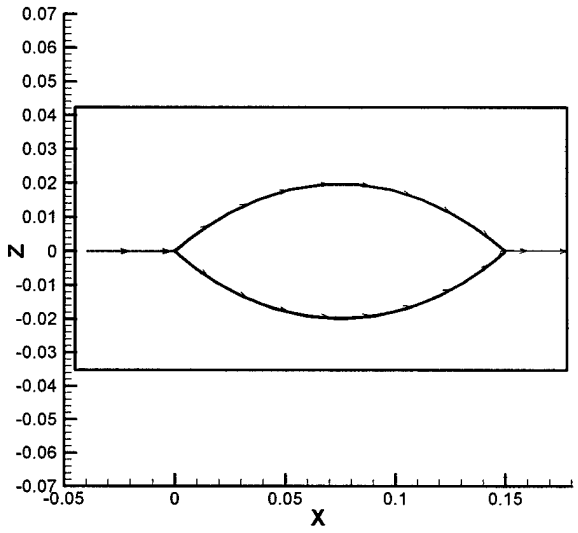

Figure 4-4: Source panel method velocity streamline results for a Biconvex blade section with $\frac{t}{D} = 0.020$ and $\alpha = 0°$ in a uniform inflow.

its robust nature to represent the blade thickness distribution at the hub and blade interface accurately.

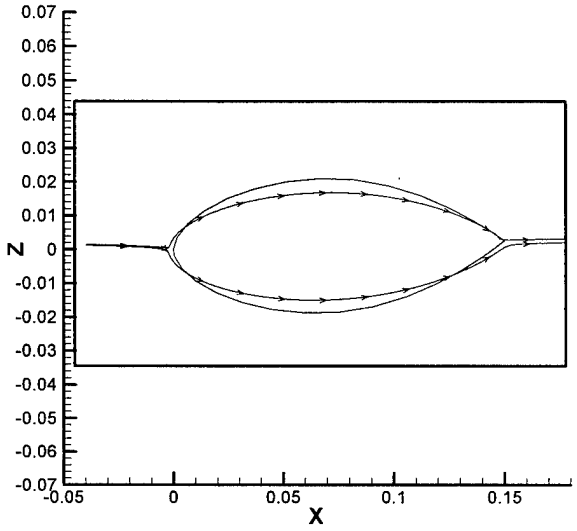

Figure 4-5: Linearized slender-body theory velocity streamline results for a NACA66 modified blade section with $\frac{t}{D} = 0.020$ and $\alpha = 1°$ in a uniform inflow.

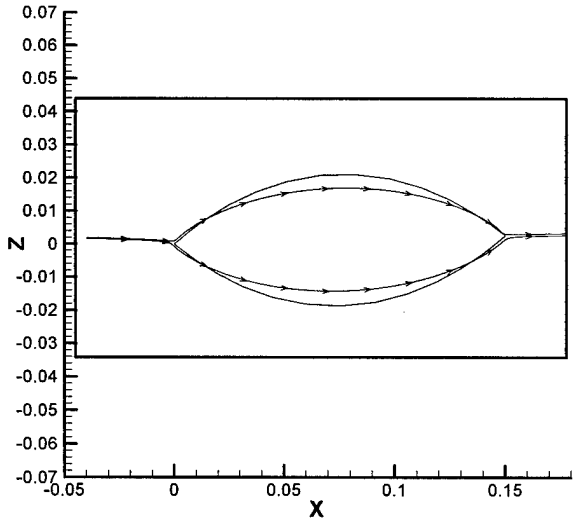

Figure 4-6: Linearized slender-body theory velocity streamline results for a NACA66 modified blade section with $\frac{t}{D} = 0.020$ and $\alpha = 1°$ in a uniform inflow.

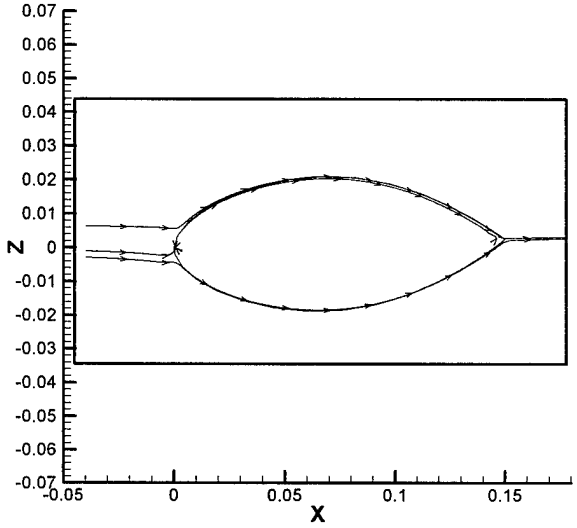

Figure 4-7: Source panel method velocity streamline results for a NACA66 modified blade section with $\frac{t}{D} = 0.020$ and $\alpha = 1°$ in a uniform inflow.

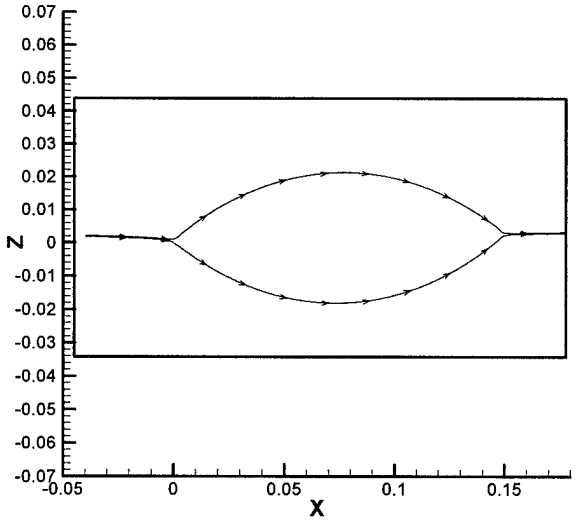

Figure 4-8: Source panel method velocity streamline results for a Biconvex blade section with $\frac{t}{D} = 0.020$ and $\alpha = 1°$ in a uniform inflow.

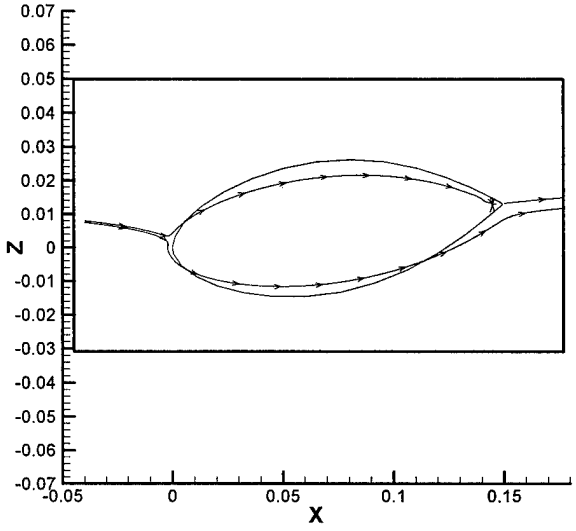

Figure 4-9: Linearized slender-body theory velocity streamline results for a NACA66 modified blade section with $\frac{t}{D} = 0.020$ and $\alpha = 5°$ in a uniform inflow.

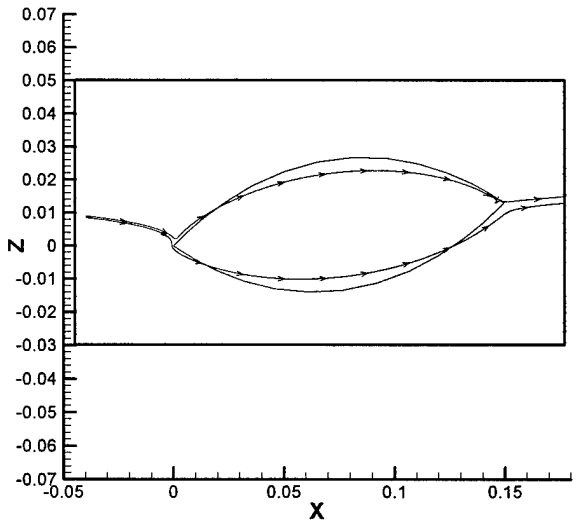

Figure 4-10: Linearized slender-body theory velocity streamline results for a Biconvex blade section with $\frac{t}{D} = 0.020$ and $\alpha = 5°$ in a uniform inflow.

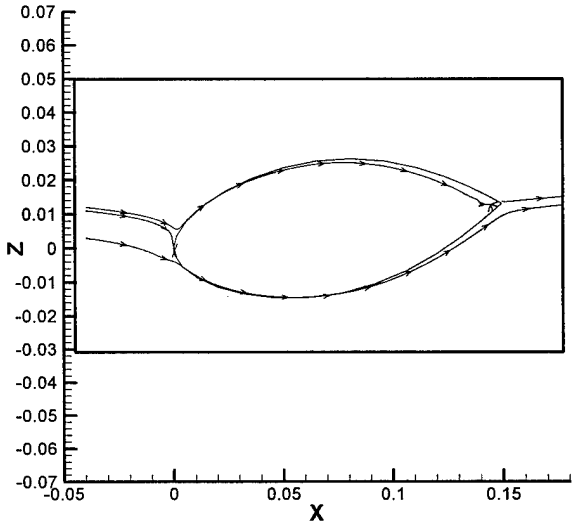

Figure 4-11: Source panel method velocity streamline results for a NACA66 modified blade section with $\frac{t}{D} = 0.020$ and $\alpha = 5°$ in a uniform inflow.

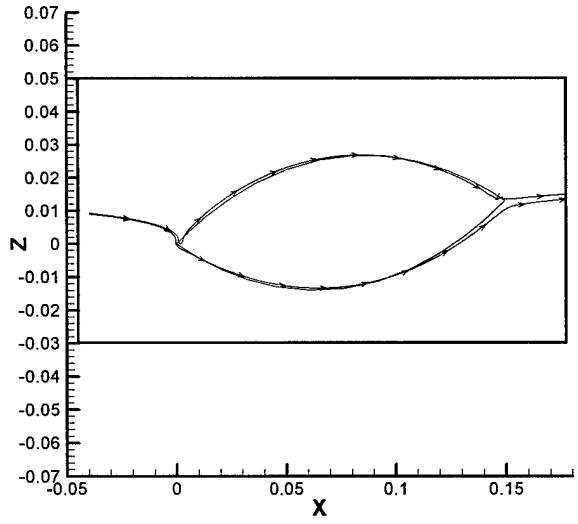

Figure 4-12: Source panel method velocity streamline results for a Biconvex blade section with $\frac{t}{D} = 0.020$ and $\alpha = 5°$ in a uniform inflow.

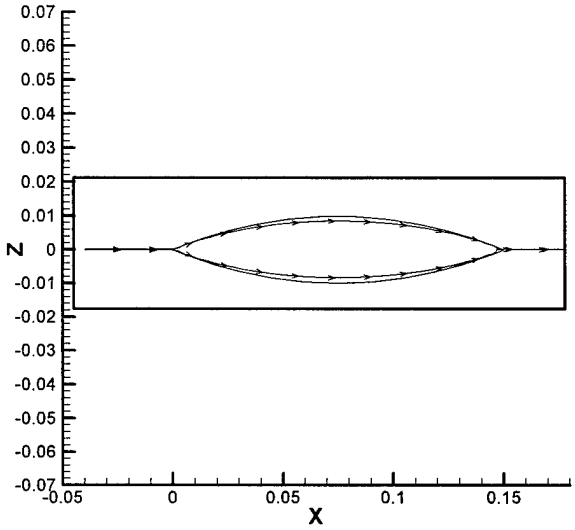

Figure 4-13: Linearized slender-body theory velocity streamline results for a Biconvex blade section with $\frac{t}{D} = 0.010$ and $\alpha = 0°$ in a uniform inflow.

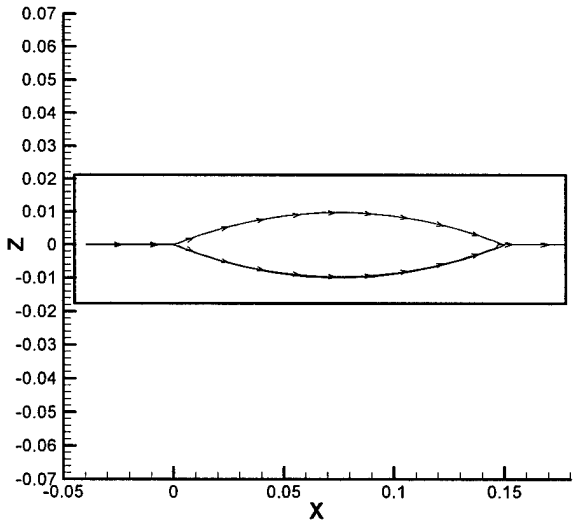

Figure 4-14: Source panel method velocity streamline results for a Biconvex blade section with $\frac{t}{D} = 0.010$ and $\alpha = 0°$ in a uniform inflow.

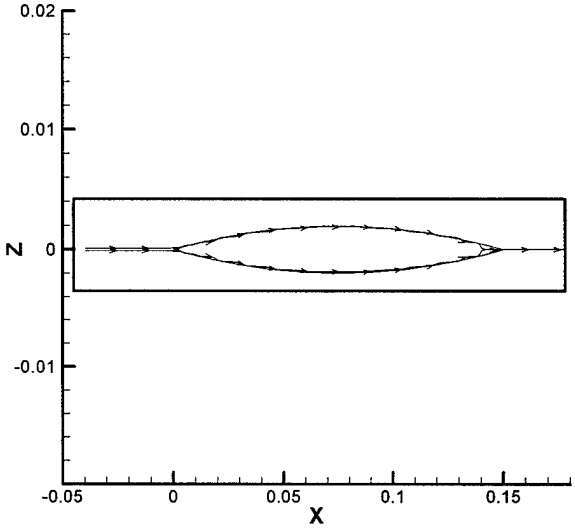

Figure 4-15: Linearized slender-body theory velocity streamline results for a Biconvex blade section with $\frac{t}{D} = 0.002$ and $\alpha = 0°$ in a uniform inflow.

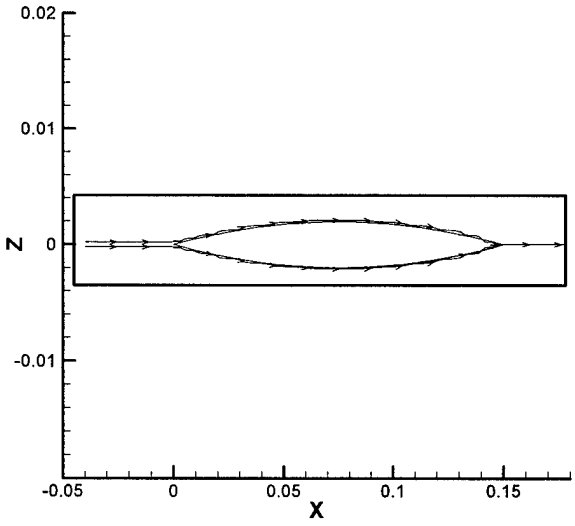

Figure 4-16: Source panel method velocity streamline results for a Biconvex blade section with $\frac{t}{D} = 0.002$ and $\alpha = 0°$ in a uniform inflow.

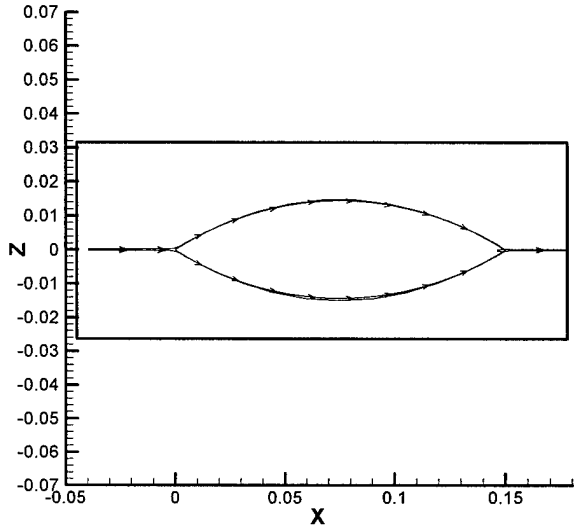

Figure 4-17: Source panel method velocity streamline results for a Biconvex blade section with $\frac{t}{D} = 0.015$ and $\alpha = 0°$ in a uniform inflow at the hub/blade interface.

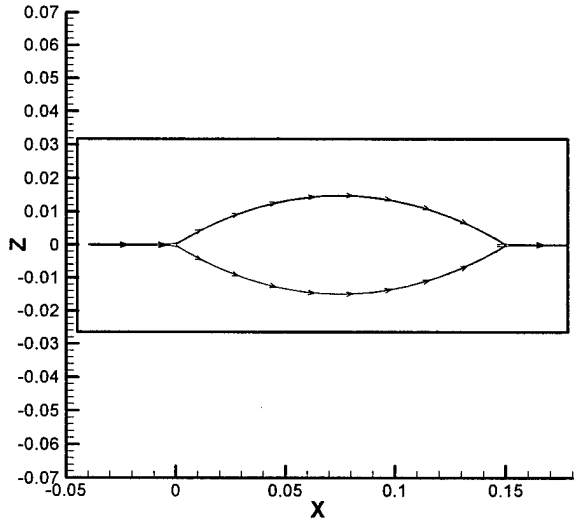

Figure 4-18: Source panel method velocity streamline results for a Biconvex blade section with $\frac{t}{D} = 0.015$ and $\alpha = 0°$ in a uniform inflow at the duct/blade interface.

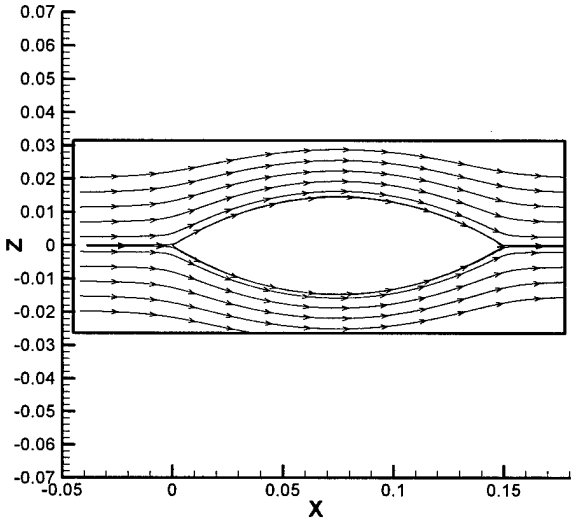

Figure 4-19: Source panel method velocity streamline results for a Biconvex blade section with $\frac{t}{D} = 0.015$ and $\alpha = 0°$ in a uniform inflow at the hub/blade interface. This streamtrace is for the key blade of an 11-blade stator system.

Chapter 5

Conclusion

5.1 Source Panel Method Results

In this thesis, several enhancements to the blade thickness representation for lifting-surface design and analysis for marine propulsors were discussed. Optimization over the whole propulsor allowed for:

- more accurate representation of the blade thickness distribution. This was accomplished by incorporating the effects of blade-to-blade interaction (blockage effect), as well as the hub-to-blade and duct-to-blade influence effects.
- still able to use the original *PBD-14* code structure to obtain solutions since the blade thickness distribution is represented by constant-strength source panels whose effect is incorporated into an overall source-induced velocity term on the right-hand side of equation 2.6.
- more accurate results for larger ranges of thickness/chord ratios and numbers of blades (cascade effect).

The weakness of the source panel method is that the computational time increases when a solution of linear equations is sought to determine the source strength distribution. Also, as a finer grid density is used to obtain more accurate results, the computational time increases.

However, this panel method enabled the kinematic boundary condition to be satisfied on the actual pressure and suction side surfaces of the blade. This ensures that $\mathbf{V}_{total}$ on the blade

surface is tangential. The hub and duct source influences, as well as other blades influences, were shown in the validation results of Chapter 4 for the following conditions:

- varying thickness/chord ratios,
- vary angles of attack and
- two distinct blade section geometries.

The velocity streamline traces showed that the source panel method is more accurate and robust over a the specified range of thickness/chord ratios, angles of attack and blade section geometries.

5.2 Recommendations for Future Enhancements

This thesis implemented a panel method into the *PBD-14* code along the mean camber surface of the vortex-lattice structure. Some recommendations for further improvements and future work in this area include:

- integrate the source panel method with the vortex lattice hub and duct formulation developed in *PBD-14.4* coding. This would allow for a more accurate representation of the hub and duct, as well as represent their associated affects on the blade thickness distribution.
- develop a more accurate field point velocity grid calculation for the entire propulsor vice just a chordwise strip to capture all three-dimensional effects visually.
- carry the source-induced velocity vector from the panel method solution to calculate a more accurate force and pressure distribution over the actual pressure and suction side surfaces of the blade.

Bibliography

[1] J.E. Kerwin and D.P. Keenan. Computational aspects of propulsor design. In *Marine Computers '91*, Burlington, MA, 1991.

[2] J.E. Kerwin and C.S. Lee. Prediction of Steady and Unsteady Marine Propeller Performance by Numerical Lifting-Surface Theory. *SNAME Transactions, 86*, 1978.

[3] D.S. Greeley and J.E. Kerwin. Numerical Methods for Propeller Design and Analysis in Steady Flow. *SNAME Transactions*, 90:415-453, 1982.

[4] J.E. Kerwin, D.P. Keenan, S.D. Black, and J.G. Diggs. A Coupled Viscous/Potential Flow Design Method for Wake-Adapted, Multi-Stage, Ducted Propulsors Using Generalized Geometry. *SNAME Transactions*, 102:23-56, 1994.

[5] J.E. Kerwin, T.E. Taylor, S.D. Black, and G. McHugh. A Coupled Lifting-Surface Analysis Technique for Marine Propulsors in Steady Flow. *Propellers/Shafting '97 Symposium*, Virginia Beach, VA, September 1997. Ship's Machinery Committee, SNAME.

[6] G.P. McHugh. Advances in Ducted propulsor Analysis Using Vortex-Lattice Lifting-Surface Techniques. Naval Engineer Thesis, Massachusetts Institute of Technology, Department of Ocean Engineering, 1997.

[7] G.P. McHugh, T.E. Taylor, W.M. Milewski, and J.E. Kerwin. PBD-14.4: A Coupled Lifting-Surface Design/Analysis Code for Marine Propulsors. Technical Report, Department of Ocean Engineering, Massachusetts of Technology, August 1998.

[8] N.J. Hahn, A.M. Polsenberg, D.H. Renick, T.E. Taylor, and J.E. Kerwin. PBD-14.3: A Coupled Lifting-Surface Design/Analysis Program for Marine Propulsors. Technical Report, Department of Ocean Engineering, Massachusetts of Technology, April 2000.

[9] S.A. Kinnas. A General Theory for the Coupling Between Thickness and Loading for Wings and Propellers. *Journal of Ship Research*, 36(1), 1992.

[10] Scott D. Black. Integrated Lifting-Surface/Navier-Stokes Design and Analysis Methods for Marine Propulsors. Master of Science Thesis, Massachusetts Institute of Technology, Department of Ocean Engineering, 1997.

[11] J. Katz and A. Plotkin. Low Speed Aerodynamics: From Wing Theory to Panel Methods, McGraw Hill Series in Aeronautical and Aerospace Engineering, 1991.

[12] J.L. Hess and A.M.O. Smith. "Calculation of Potential Flow About Arbitrary Bodies," *Progress in Aeronautical Sciences*, vol. 8, pp. 1-138, 1967

Appendix A

Constant-Strength Quadrilateral Source Distribution Formulation

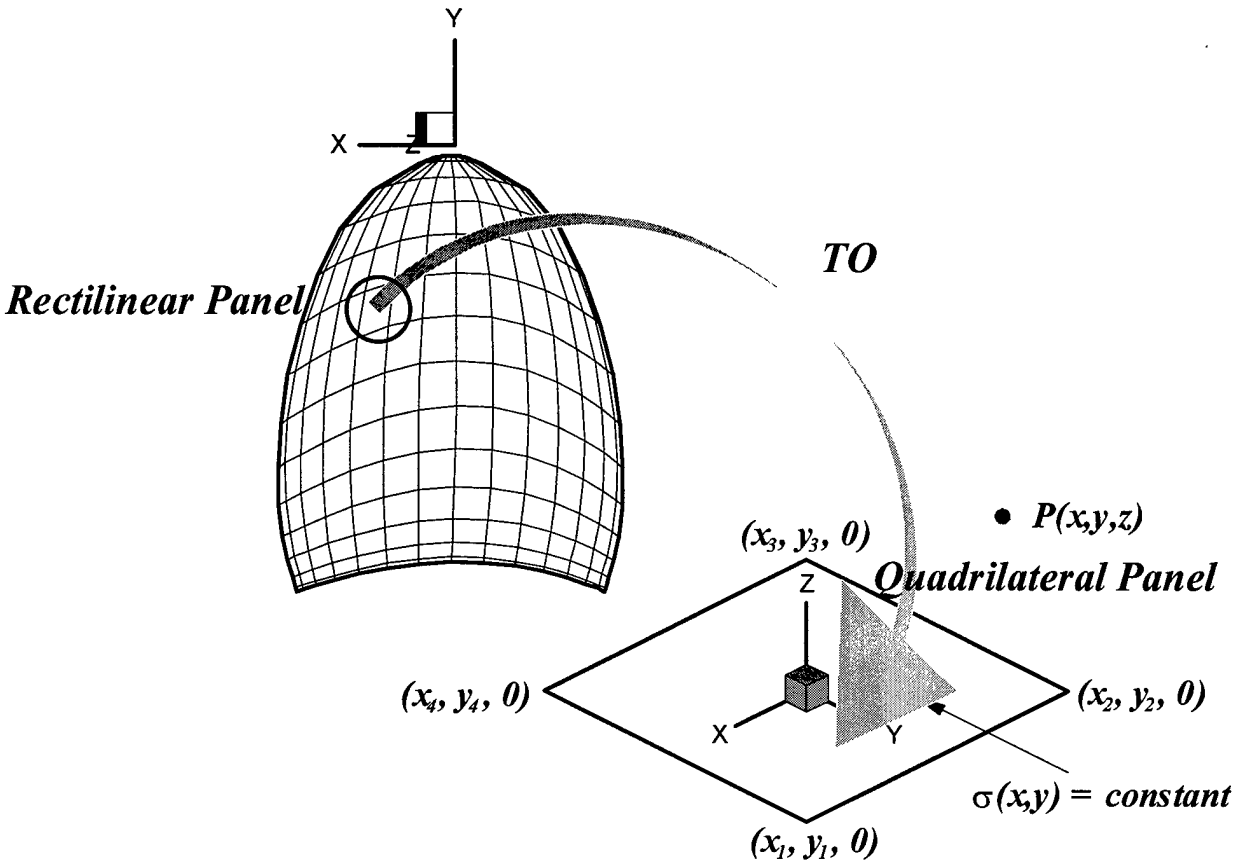

Figure A-1: Rectilinear to Quadrilateral constant-strength source panel transformation.

Consider a surface element ($z = constant$) with a constant-strength source distribution, σ_A, per area, bounded by four straight lines as described in Figure A-1. The potential at an arbitrary point $P(x, y, z)$, due to this element is

$$\Phi(x, y, z) = -\frac{\sigma_A}{4\pi} \int_S \frac{dS}{\sqrt{(x - x_0)^2 + (y - y_0)^2 + z^2}} \tag{A.1}$$

and the velocity components can be obtained by differentiating the velocity potential:

$$(u, v, w) = (\frac{\partial \Phi}{\partial x}, \frac{\partial \Phi}{\partial y}, \frac{\partial \Phi}{\partial z}) \tag{A.2}$$

A.1 Near Field Formulation

Execution of the integration within the area bounded by the four straight lines requires a lengthy process. The details of integration are shown in reference [12] and the results obtained for the potential of a planar element becomes

$$\Phi(x,y,z) = -\frac{\sigma_A}{4\pi}\left\{\begin{array}{l}\left[\begin{array}{l}\frac{(x-x_1)(y-y_1)-(y-y_1)(x_2-x_1)}{d_{12}}\ln\frac{r_1+r_2+d_{12}}{r_1+r_2-d_{12}}\\ +\frac{(x-x_2)(y_3-y_2)-(y-y_2)(x_3-x_2)}{d_{23}}\ln\frac{r_2+r_3+d_{23}}{r_2+r_3-d_{23}}\\ +\frac{(x-x_3)(y_4-y_3)-(y-y_3)(x_4-x_3)}{d_{34}}\ln\frac{r_3+r_4+d_{34}}{r_3+r_4-d_{34}}\\ +\frac{(x-x_4)(y_1-y_4)-(y-y_4)(x_1-x_4)}{d_{41}}\ln\frac{r_4+r_1+d_{41}}{r_4+r_1-d_{41}}\end{array}\right]\\ +|z|\left[\begin{array}{l}\tan^{-1}\left(\frac{m_{12}e_1-h_1}{zr_1}\right)-\tan^{-1}\left(\frac{m_{12}e_2-h_2}{zr_2}\right)\\ +\tan^{-1}\left(\frac{m_{23}e_2-h_2}{zr_2}\right)-\tan^{-1}\left(\frac{m_{23}e_3-h_3}{zr_3}\right)\\ +\tan^{-1}\left(\frac{m_{34}e_3-h_3}{zr3}\right)-\tan^{-1}\left(\frac{m_{34}e_4-h_4}{zr_4}\right)\\ +\tan^{-1}\left(\frac{m_{41}e_4-h_4}{zr_4}\right)-\tan^{-1}\left(\frac{m_{41}e_1-h_1}{zr_1}\right)\end{array}\right]\end{array}\right\} \tag{A.3}$$

where

$$d_{12} = \sqrt{(x_2-x_1)^2+(y_2-y_1)^2} \tag{A.4}$$

$$d_{23} = \sqrt{(x_3-x_2)^2+(y_3-y_2)^2} \tag{A.5}$$

$$d_{34} = \sqrt{(x_4-x_3)^2+(y_4-y_3)^2} \tag{A.6}$$

$$d_{41} = \sqrt{(x_1-x_4)^2+(y_1-y_4)^2} \tag{A.7}$$

and

$$m_{12} = \frac{y_2-y_1}{x_2-x_1} \tag{A.8}$$

$$m_{23} = \frac{y_3-y_2}{x_3-x_2} \tag{A.9}$$

$$m_{34} = \frac{y_4 - y_3}{x_4 - x_3} \tag{A.10}$$

$$m_{41} = \frac{y_1 - y_4}{x_1 - x_4} \tag{A.11}$$

and

$$r_k = \sqrt{(x - x_k)^2 + (y - y_k)^2 + z^2} \tag{A.12}$$

$$e_k = (x - x_k)^2 + z^2 \tag{A.13}$$

$$h_k = (x - x_k)(y - y_k) \tag{A.14}$$

where $k = 1, 2, 3, 4$.

The velocity components, based on the results from Hess and Smith [12] are

$$u = \frac{\sigma_A}{4\pi} \left[\begin{array}{c} \frac{y_2 - y_1}{d_{12}} \ln \frac{r_1 + r_2 - d_{12}}{r_1 + r_2 + d_{12}} + \frac{y_3 - y_2}{d_{23}} \ln \frac{r_2 + r_3 - d_{23}}{r_2 + r_3 + d_{23}} \\ + \frac{y_4 - y_3}{d_{34}} \ln \frac{r_3 + r_4 - d_{34}}{r_3 + r_4 + d_{34}} + \frac{y_1 - y_4}{d_{41}} \ln \frac{r_4 + r_1 - d_{41}}{r_4 + r_1 + d_{41}} \end{array} \right] \tag{A.15}$$

$$v = \frac{\sigma_A}{4\pi} \left[\begin{array}{c} \frac{x_1 - x_2}{d_{12}} \ln \frac{r_1 + r_2 - d_{12}}{r_1 + r_2 + d_{12}} + \frac{x_2 - x_3}{d_{23}} \ln \frac{r_2 + r_3 - d_{23}}{r_2 + r_3 + d_{23}} \\ + \frac{x_3 - x_4}{d_{34}} \ln \frac{r_3 + r_4 - d_{34}}{r_3 + r_4 + d_{34}} + \frac{x_4 - x_1}{d_{41}} \ln \frac{r_4 + r_1 - d_{41}}{r_4 + r_1 + d_{41}} \end{array} \right] \tag{A.16}$$

$$w = \frac{\sigma_A}{4\pi} \left[\begin{array}{c} \tan^{-1}\left(\frac{m_{12}e_1 - h_1}{zr_1}\right) - \tan^{-1}\left(\frac{m_{12}e_2 - h_2}{zr_2}\right) + \tan^{-1}\left(\frac{m_{23}e_2 - h_2}{zr_2}\right) - \tan^{-1}\left(\frac{m_{23}e_3 - h_3}{zr_3}\right) \\ + \tan^{-1}\left(\frac{m_{34}e_3 - h_3}{zr3}\right) - \tan^{-1}\left(\frac{m_{34}e_4 - h_4}{zr_4}\right) + \tan^{-1}\left(\frac{m_{41}e_4 - h_4}{zr_4}\right) - \tan^{-1}\left(\frac{m_{41}e_1 - h_1}{zr_1}\right) \end{array} \right] \tag{A.17}$$

The u and v components of the velocity are defined everywhere but at the edges of the quadrilateral, where they become infinite. If the influence of the element on itself is sought, then these velocity components approach zero near the centroid. The jump in the normal velocity component as $z \longrightarrow 0$ inside the quadrilateral is

$$w(z = 0\pm) = \pm\frac{\sigma_A}{2}. \tag{A.18}$$

When the point on interest P (z = *constant*) lies outside of the quadrilateral, then

$$w(z = 0\pm) = 0. \tag{A.19}$$

A subroutine was written to incorporate code to handle nonplanar panels. Basically any rectilinear panel is input into this subroutine which then adjusts the panel dimensions to correctly represent it as a quadrilateral panel with a $x-y$ planar surface on a constant $z-surface$. This subroutine also calculates the center of the rectilinear panel which maintains the orientation between the local (panel) and global (blade geometry) coordinate systems.

A.2 Far Field Formulation

For improved computational efficiency, when the point of interest P is far from the center of the element (x_0, y_0,z = *constant*) then the influence of the quadrilateral element with an area of A can be approximated by a point source. When the term "far" is invoked, that is a distance more than five average panel characteristic lengths (longest distance between any two endpoints), then a simplified approximation is used. The point source influence for the velocity potential becomes

$$\Phi(x, y, z) = -\frac{\sigma_A A}{4\pi\sqrt{(x - x_0)^2 + (y - y_0)^2 + z^2}} \tag{A.20}$$

The velocity components of this source element are

$$u = \frac{\sigma_A A(x - x_0)}{4\pi\left[(x - x_0)^2 + (y - y_0)^2 + z^2\right]^{3/2}} \tag{A.21}$$

$$v = \frac{\sigma_A A(y - y_0)}{4\pi\left[(x - x_0)^2 + (y - y_0)^2 + z^2\right]^{3/2}} \tag{A.22}$$

$$w = \frac{\sigma_A A(z - z_0)}{4\pi\left[(x - x_0)^2 + (y - y_0)^2 + z^2\right]^{3/2}}. \tag{A.23}$$

An algorithm for calculating the influence of a quadrilateral constant strength source element (Program 11) was used [11].

Appendix B

Infinite-Pitch Stator *PBD-14* Input File

PBD-14.3 admin file for Infinite-pitch stator DSH 6/5/00										
stator.bsn										:File name for blade b-spline net
samp.vel										:File name for wake field
1	15	15								:nblade, nkey, mkey
1	1									:ispn (0=uniform,1=cos),iffixlat
14	1,2,	...,	40							:mctrp,mc(n)
7	0.0	7	0.0							:ihub, hgap, iduct, dgap
0	0									:IHUB_SUBLAY, IDUC_SUBLAY
10	8									:HDWAK, NTWAKE
0.84	300									:Cq, MXITER
0.3	0.3									:OVHANG(1), OVHANG(3)
10	-10	0	8							:nx, ngcoeff, mltype, mthick
4										:IMODE
0										:NXIMAX
5	.001	.02	5.	1						:niter, tweak, bulge, radwgt, nufix
1	.08									:nplot, hubshk
4	2									:NOPT, NBLK
999.	1.0	1.5	.05							:ADVCO, XULT, XFINAL, DTPROP
.0	.0	.0	.0	.0	.0	.0	.0	.0	.0	:G
.2	.3	.4	.5	.6	.7	.8	.9	.95	1.0	:r/R
.015	.015	.015	.015	.015	.015	.015	.015	.015	.015	:t/D
.0	.0	.0	.0	.0	.0	.0	.0	.0	.0	:Cd

Table B.1: Sample input file for PBD-14.